Supporting Information for CrystEngComm 2021

Two robust Zn(II)-organic frameworks as dual-functional fluorescent probes for efficient sensing of enrofloxacin and MnO_4^- anions

Yu-Qiao Su[a], Ruo-Tong Wang[a], Olga A. Blatova[b], Yong-Sheng Shi[a],

Guang-Hua Cui[a]*

[a]*College of Chemical Engineering, Hebei Key Laboratory for Environment Photocatalytic and Electrocatalytic Materials, North China University of Science and Technology, No. 21 Bohai Road, Caofeidian new-city, Tangshan, Hebei, 063210, P. R. China*

[b]*Samara Center for Theoretical Materials Science (SCTMS), Samara State Technical University, Molodogvardeyskaya St. 244, 443100 Samara, Russian Federation.*

Corresponding author: Guang-Hua Cui

Fax: +86-315-8805462. Tel: +86-315-8805460.

E-mail: tscghua@126.com

CONTENTS

Section 1. Computational Details

1. Materials and methods

2. Single-crystal X-ray structure determination of **1**−**2**

3. Computational details

1. Materials and methods

L1−L2 were collected from Jinan Henghua Sci. & Tec. Co. Ltd. (Jinan, China). The others chemicals and reagents were purchased and could be used without further purification. On a Rigaku D/Max-2500 X-ray powder diffractometer (Cu-Kα, 1.5418 Å), powder X-ray diffraction (PXRD) patterns were carried out. In the 4000 to 400 cm^{-1} area, the FT-IR spectra were recorded from a Bruker VERTEX 80V FT-IR spectrophotometer. Elemental tests (C, H, and N) were conducted on the elemental analyzer PerkinElmer 240 C. A NETZSCH TG 209 thermal analyzer in air was used to collect thermogravimetric analysis (TGA) data at a heating rate of 10 °C min^{-1} in the 25−700 °C range. Ultrasonic irradiation was carried out in an ultrasonic bath KQ-300DE (40 kHz, Sonicator Company, Kunshan, China). The solid-state fluorescent assay was performed using an Edinburgh FS5 fluorescence spectrophotometer at room temperature.

2. Single crystal X-ray diffraction determination of 1−2

The single-crystal structure data of **1**−**2** were obtained at room temperature on a Rigaku XtaLabMini diffractometer fitted with Mo-Kα radiation ($\lambda = 0.71073$ Å), using the CrysAlisPro software to record the reflection data.[1] Structural analysis and data refinement were performed through the SHELXT-2015 and SHELXL-2018 programs.[2–4] From differential Fourier charts, all ordered non-hydrogen atoms were found and refined with anisotropic thermal parameters. The H atoms of organic ligands are technically produced and isotropically refined with fixed thermal factors. The H atoms in water molecules were added by difference Fourier maps and with fixed displacement parameters.[5] **Table S1** summarizes crystallographic details and structure refinement parameters for **1**−**2**. Selected bond lengths and bond angles are shown in **Table S2**.

3. Computational Details

All calculations on electronic structures were carried out *via* ORCA 2.8 program.[6] Geometry optimizations was calculated through density functional theory (DFT). The frontier orbital energy of Zn(II) ions, free L1 and L2, and H_2NDC were calculated by B3LYP/TZVP.[7–9] Molecular orbital visualization was analyzed by VMD 1.9.3 program.[10] The structural properties of the two Zn(II)-MOFs were calculated by Poreblazer v4.0 program (**Table S4**).[11]

References

[1] Agilent. CrysAlis PRO. Agilent Technologies Ltd, Yarnton, Oxfordshire, England, 2014.

[2] O. V. Dolomanov, L. J. Bourhis, R. J, Gildea, J. A. K. Howard, J.A.K., H. Puschmann, *J. Appl. Cryst*. 2020, **42**, 339−341.

[3] L. J. Bourhis, O. V. Dolomanov, R. J, Gildea, J. A. K. Howard, H. Puschmann, *Acta Cryst*. 2020, **A71**, 59−75.

[4] G. M. Sheldrick, *Acta Crystallogr., Sect. C: Cryst. Struct. Commun*., 2015, **71**, 3−8.

[5] A. L. Spek, *Acta Crystallogr.*, *Sect. D*, 2009, **65**, 148−155.

[6] F. Neese, Wiley Interdiscip. Rev. Sci., 2012, 2, 73−78.

[7] A. D. Becke, J. Chem. Phys., 1993, 5648.

[8] A. D. Becke, Phys. Rev., 1988, 38, 3098.

[9] O. Treutler, Re. Ahlrichs, J. Chem. Phys., 1995, 102, 346−354.

[10] W. Humphrey, A. Dalke, K. Schulten, J. Mol. Graphics, 1996, 14, 33−38.

[11] L. Sarkisov, R. B. Perez, M. Sutharson, D. F. Jimenez, Chem. Mater, 2020, 32, 9849−9867.

Section 2. Supplementary Schemes and Tables

Scheme Titles:

Scheme S1 Structure formulas of L1–L2 ligands.

Scheme S2 The structure formulas of different types of antibiotics.

Table Titles:

Table S1 Crystal data and structure refinements for the **1−2**.

Table S2 Selected Bond Lengths [Å] and Angles [º] for the **1**–**2**.

Table S3 Thermal stability analysis for **1**–**2**.

Table S4. Comparison of the sensitivities of **1**–**2** with previously reported MOFs to enrofloxacin.

Table S5. Comparison of the sensitivities of **1**–**2** with previously reported MOFs to MnO_4^-.

Table S6 The structural properties for **1** and **2**.

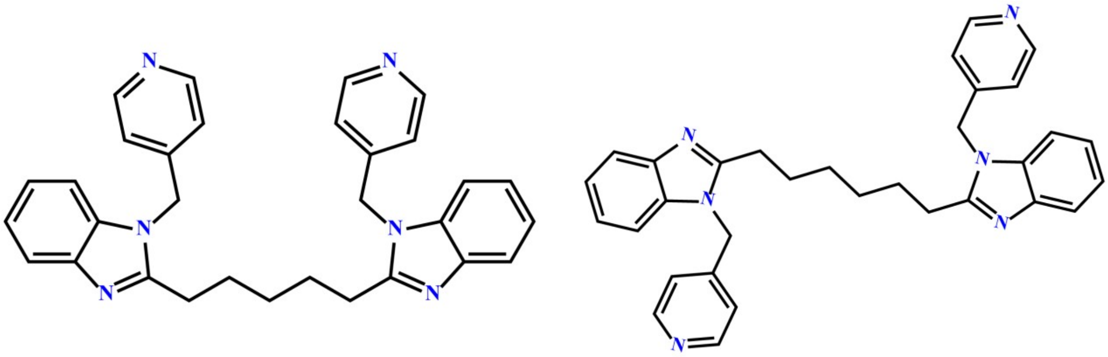

L1 **L2**

Scheme S1 Structure formulas of L1–L2 ligands.

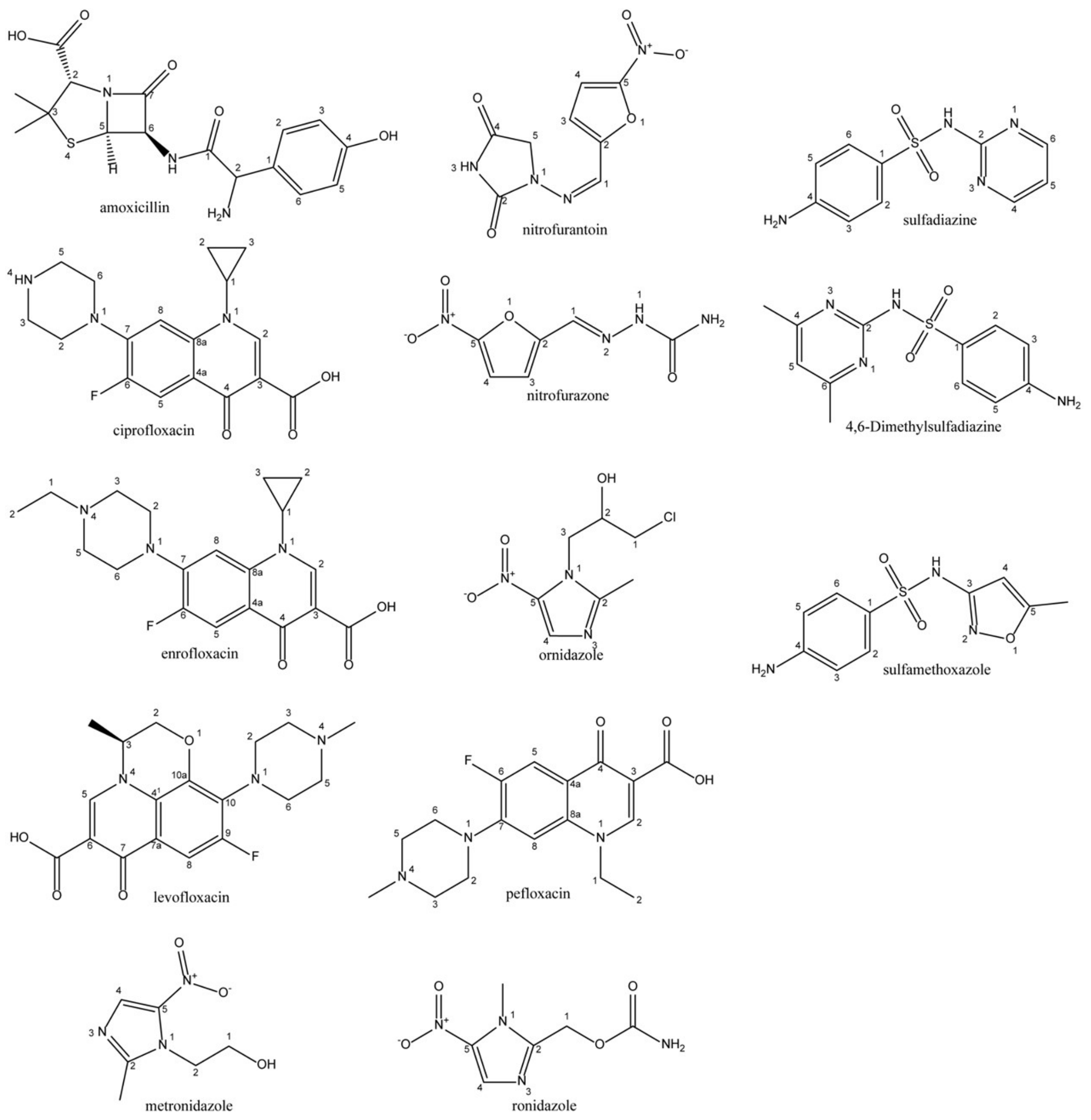

Scheme S2 The structure formulas of different types of antibiotics.

Table S1 Crystal data and structure refinements for the **1−2**

MOF	**1**	**2**
Chemical formula	$C_{123}H_{93}N_{12}O_{22.5}Zn_6$	$C_{44}H_{42}N_6O_6Zn$
Formula weight	2491.44	816.20
Crystal system	triclinic	monoclinic
Space group	$P\bar{1}$	$P2_1/c$
a (Å)	10.8732(6)	17.8383(5)
b (Å)	15.9024(9)	14.9191(3)
c (Å)	17.0471(7)	16.6035(5)
α (°)	105.733(4)	90
β (°)	103.099(4)	108.071(3)
γ (°)	91.265(4)	90
V (Å^3)	2751.8(3)	3974.2(2)
Z	1	4
D_{calcd} (g/cm^3)	1.052	1.364
Absorption coefficient, mm^{-1}	1.366	0.675
F(000)	1273	1704
Crystal size, mm	0.20 x 0.16 x 0.12	0.23 x 0.21 x 0.19
θ range, deg	4.496–52.042	4.962–61.17
Index range h, k, l	–15/15, –22/22, –24/24	–23/23, –21/21, –23/23
Reflections collected	61585	59753
Independent reflections (R_{int})	10763 (0.0370)	11817(0.0735)
Data/restraint/parameters	16074 / 280 / 813	11817 / 0 / 520
Goodness-of-fit on F^2	1.117	1.060
Final R_1, wR_2 ($I > 2\sigma(I)$)	0.0424, 0.1056	0.0709, 0.1100
Largest diff. peak and hole	0.61, –0.58	0.44, –0.36

Table S2 Selected Bond Lengths [Å] and Angles [º] for the **1**–**2**

Parameter	Value	Parameter	Value
1			
Zn1–O2	1.965(2)	Zn1–O11	1.905(2)
Zn1–O6	1.928(2)	Zn1–N1	1.995(2)
Zn2–O1	2.261(2)	Zn2–O11	2.149(3)
Zn2–O5	2.072(2)	Zn2–N6E	2.600(3)
Zn2–O9	2.026(2)	Zn3–O3A	2.017(2)
Zn3–O4B	2.068(2)	Zn3–O7C	2.052(2)
Zn3–O8D	2.055(2)	Zn3–N4	2.021(2)
O2–Zn1–O6	105.38(10)	O2–Zn1–N1	113.28(9)
O6–Zn1–N1	102.58(9)	O11–Zn1–O2	110.19(10)
O11–Zn1–O6	107.52(9)	O11–Zn–N1	116.8(9)
O9–Zn2–O1	86.21(9)	O9–Zn2–O5	93.35(8)
O9–Zn2–N6E	88.54(10)	O11–Zn2–O1	90.61(8)
O11–Zn2–O5	102.21(8)	O11–Zn2–O9	161.91(9)
O11–Zn2–N6E	94.87(10)	N6E–Zn2–O1	174.52(9)
O3A–Zn3–O4B	156.24(11)	O3A–Zn3–O7C	88.97(13)
O3A–Zn3–O8D	88.08(13)	O3A–Zn3–N4	106.90(11)
O7C–Zn3–O4B	87.75(12)	O7C–Zn3–O8D	156.74(9)
O8D–Zn3–O4B	85.73(11)	N4–Zn3–O4B	96.82(10)
N4–Zn3–O7C	101.06(9)	N4–Zn3–O8D	101.88(10)
2			
Zn1–O1	1.965(2)	Zn1–N1	2.057(2)
Zn1–O4A	1.983(2)	Zn1–N4B	2.074(2)
O1–Zn1–O4A	125.53(8)	O4A–Zn1–N1	109.81(8)
O1–Zn1–N1	106.68(8)	O4A–Zn1–N4B	102.24(8)
O1–Zn1–N4B	110.19(8)	N4B–Zn1–N1	99.31(8)

symmetry code: A: −1+*x*, *y*, *z*, B: 1−*x*, 2−*y*, 2−*z*, C: −1+*x*, 1+*y*, *z*, D: 1−*x*, 1−*y*, 2−*z*, E: 1−*x*, 1−*y*, 1−*z* for **1.** A: *x*, 0.5−*y*, 0.5+*z*, B: *x*, 1.5−*y*, −0.5+*z* for **2**

Table S3 Thermal stability analysis for **1**–**2**

MOF	Loss of matter	Decomposition temperature/°C	Experimental value/%	Theoretical value/%
1	H_2O/$NDC^{2-}$and L1	26~126/320~550	1.81/78.60	1.84/78.74
2	H_2O/NDC^{2-} and L2	34~100/310~530	4.41/85.62	3.90/85.88

Table S4. Comparison of the sensitivities of **1**–**2** with previously reported MOFs to enrofloxacin

MOF	Types	LOD/mol/L	Ref
$[Cd(H_2L)(H_2O)_3]\cdot NMP$	enrofloxacin	2.50×10^{-8}	[11]
Eu(2,6-NDC)(COO)	enrofloxacin	0.12×10^{-6}	[14]
1	enrofloxacin	7.06×10^{-10}	This work
2	enrofloxacin	2.89×10^{-9}	This work

H_4L = [1,1’:4’,1”-terphenyl]- 2’,3,3”,5’-tetracarboxylic acid; 2,6-NDC = 2,6-naphthalenedicarboxylic acid.

Table S5. Comparison of the sensitivities of **1**–**2** with previously reported MOFs to MnO_4^-

MOF	Types	LOD/mol/L	Ref
$[Zn(5\text{-}NH_2\text{-}1,3\text{-}bdc)(H_2O)]$	MnO_4^-	1.280×10^{-6}	[4]
$[Zn_2(5\text{-}NH_2\text{-}1,3\text{-}bdc)_2(NI\text{-}bpy\text{-}44)]\cdot DMF$	MnO_4^-	1.050×10^{-6}	[4]
$[Zn_2(BDC)_{1.5}(L)(DMF)]\cdot 1.5DMF$	MnO_4^-	0.030×10^{-6}	[5]
$(Eu_{0.06}Tb_{0.04}Gd_{0.9}\text{-}DPNC)_n$	MnO_4^-	0.020×10^{-6}	[6]
$\{[Zn_6Cl_6(2,2'\text{-}dbpt)_3]\cdot 6H_2O\}_n$	MnO_4^-	6.140×10^{-6}	[8]
1	MnO_4^-	0.286×10^{-6}	This work
2	MnO_4^-	0.507×10^{-6}	This work

$5\text{-}NH_2\text{-}1,3\text{-}H_2bdc$ = 5-amino-1,3-benzenedicarboxylic acid, NI-bpy-44 = N-(pyridin-4-yl)-4-(pyridin-4-yl)-1,8-naphthalimide; L = pyridine 4-carboxylic acid, BDC = benzene-1,4-dicarboxylate; H_3DPNC = 5-(3',5'-dicarboxylphenyl) nicotinic acid; $2,2'\text{-}H_2dpbt$ = 5,5'-di(pyridin-2-yl)-3,3'-bi(1,2,4-triazole).

Table S6 The structural properties for **1** and **2**

property	**1**	**2**
accessible surface area, m^2/g	6535.03	11491.01
geometric pore volume, cm^3/g	1.67	3.43
probe-occupiable volume, cm^3/g	1.60	3.37
helium pore volume, cm^3/g	1.37	3.00
pore limiting diameter, Å	6.06	7.45
largest cavity diameter, Å	8.64	9.74

Section 3. Supplementary Figures

Fig. S1. (a) Coordination geometry of Zn^{2+} ions in **1**; (b) View of the coordination modes of NDC^{2-} anions in **1** (c) The three-dimensional structure formation process for **1**.

Fig. S2. (a) Coordination geometry of Zn^{2+} ions in **2**; (b) The two-dimensional structure formation process for **2**; (c) In **2**, the simplification of NDC^{2-} and L2 ligand and the specific formation process of **sql** topological structure.

Fig. S3. (a) Simulated and experimental PXRD patterns of **1**–**2**; (b) PXRD patterns of **1** and **2** under different conditions.

Fig. S4. The change of the fluorescence emission intensities of **1**–**2** in different pH solutions.

Fig. S5. TGA curves of **1**–**2.**

Fig. S6 Time resolved luminescence decay of **1** and **2**.

Fig. S7. The plot of relative **1**–**2** luminescence intensities *vs* enrofloxacin (ENR) concentration.

Fig. S8. Time-dependent emission spectra of **1**–**2** with ENR (0.25 μmol/L) at the different reaction time.

Fig. S9. The correlation curves between $[(I_0/I) - 1]$ and the concentration of MnO_4^- obtained by the Stern−Volmer equation.

Fig. S10. The time required for the quenching efficiencies of **1**/**2**@MnO_4^- anions to reach the maximum.

Fig. S11. Comparison of the quenching efficiencies of **1**–**2** for sensing of ENR/MnO_4^- anions over four cycles.

Fig. S12. PXRD patterns of **1**–**2** after 4 cycles of detecting of ENR/MnO_4^- anions

Fig. S13. Fluorescence excitation spectra of **1**/**2** and UV–vis absorption spectrum of enrofloxacin.

Fig. S14. Spectral overlap between the absorption spectrum of MnO_4^- anions and the excitation spectra of **1**–**2**.

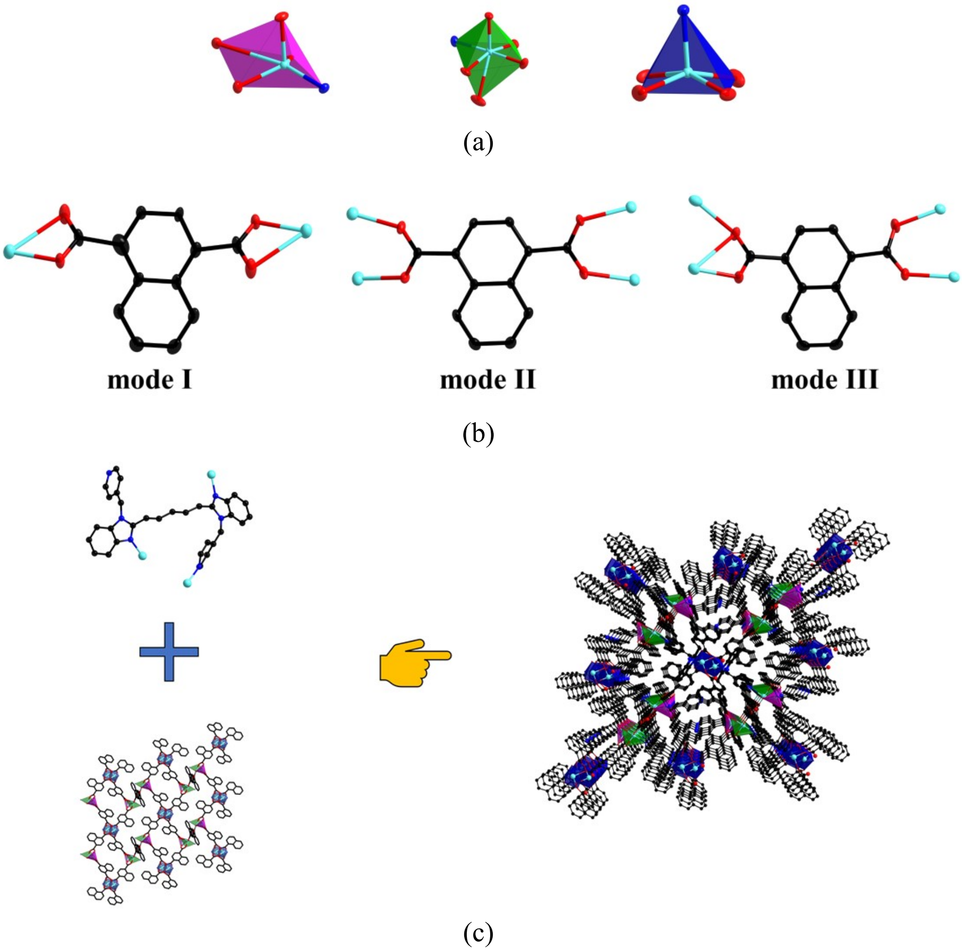

Fig. S1. (a) Coordination geometry of Zn^{2+} ions in **1**; (b) View of the coordination modes of NDC^{2-} anions in **1** (c) The three-dimensional structure formation process for **1**.

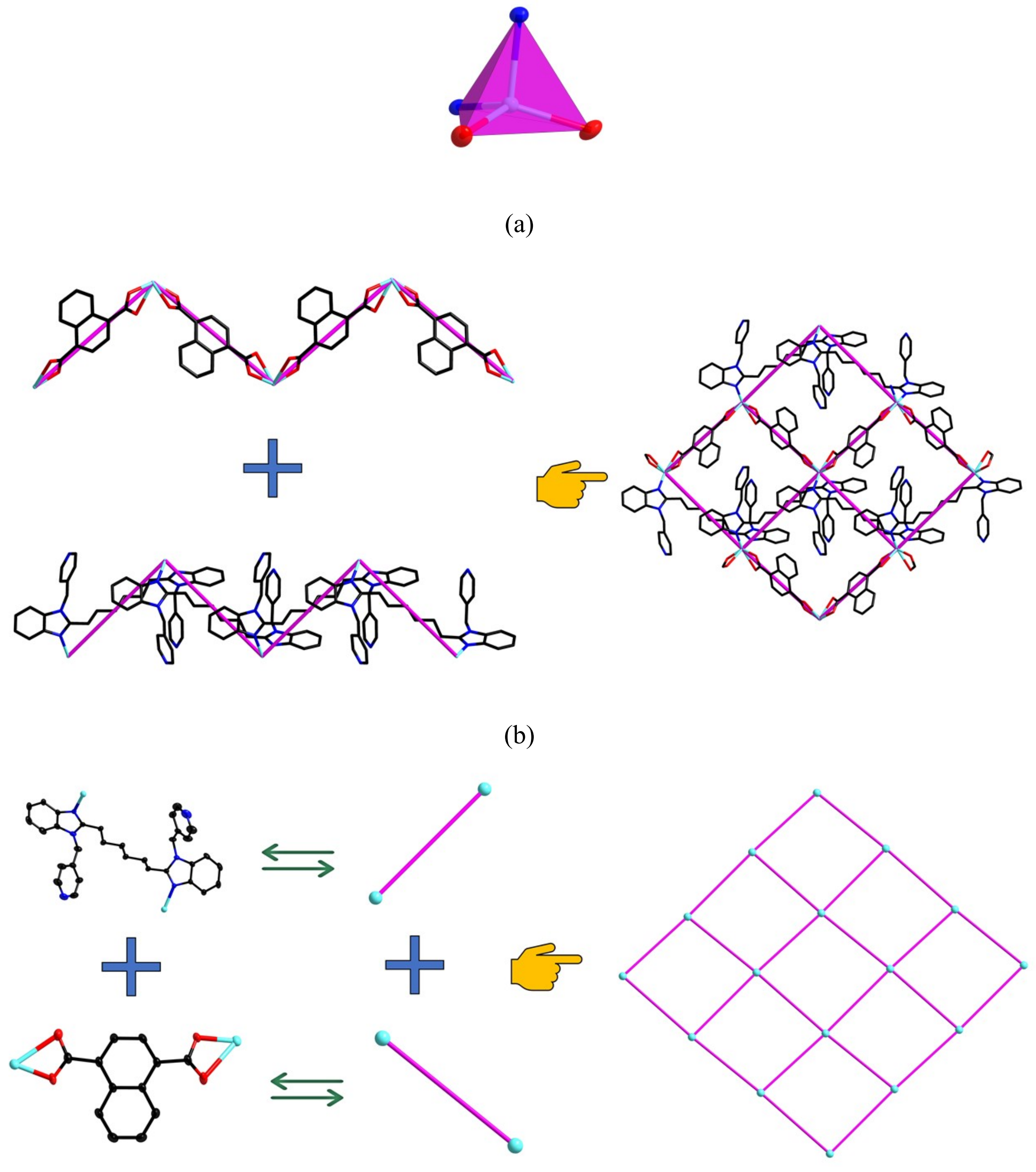

(a)

(b)

(c)

Fig. S2. (a) Coordination geometry of Zn^{2+} ions in **2**; (b) The two-dimensional structure formation process for **2**; (c) In **2**, the simplification of NDC^{2-} and L2 ligand and the specific formation process of **sql** topological structure.

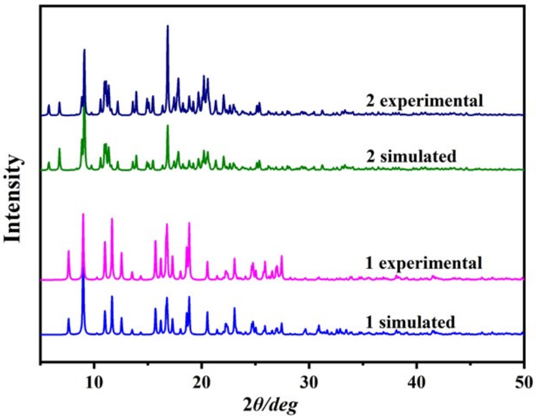

(a)

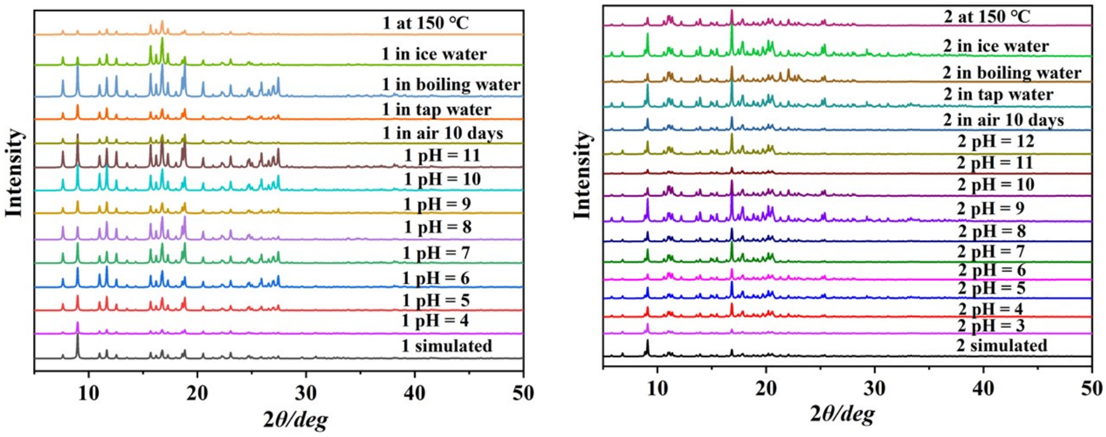

(b)

Fig. S3. (a) Simulated and experimental PXRD patterns of **1**–**2**; (b) PXRD patterns of **1** and **2** under different conditions.

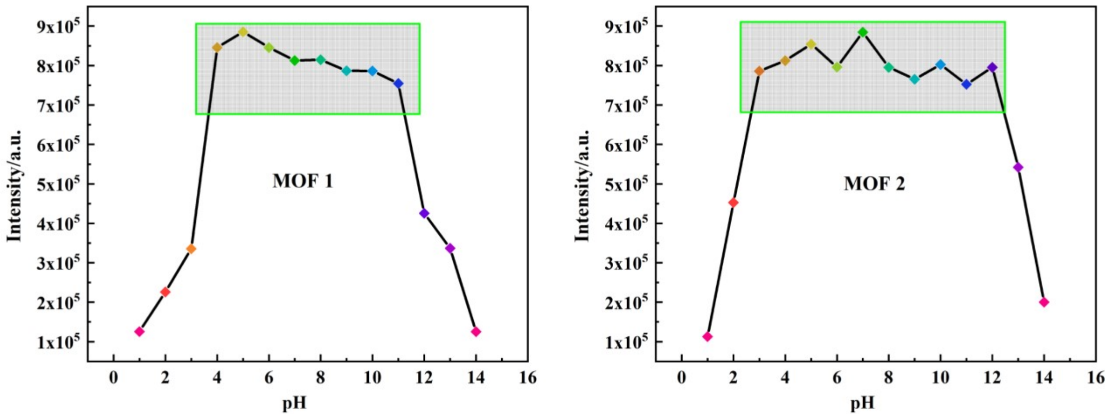

Fig. S4. The change of the fluorescence emission intensities of **1**–**2** in different pH solutions.

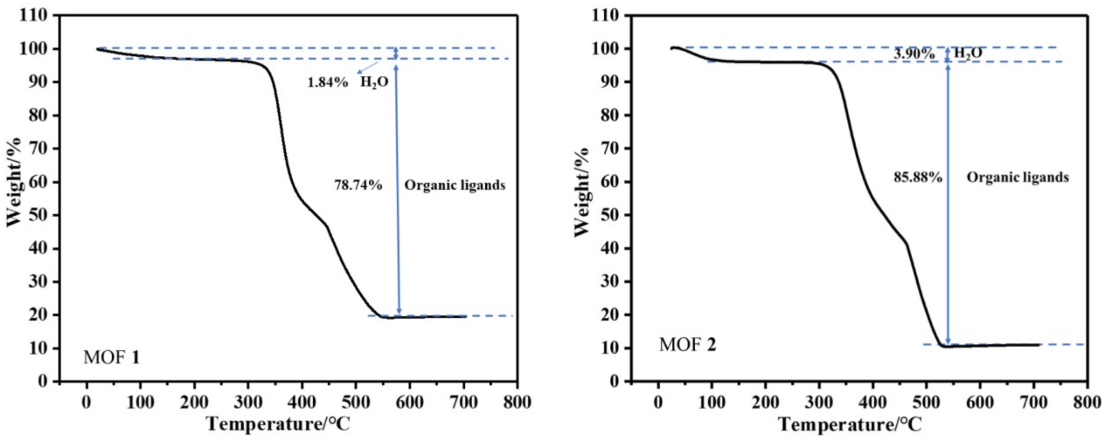

Fig. S5. TGA curves of **1**–**2.**

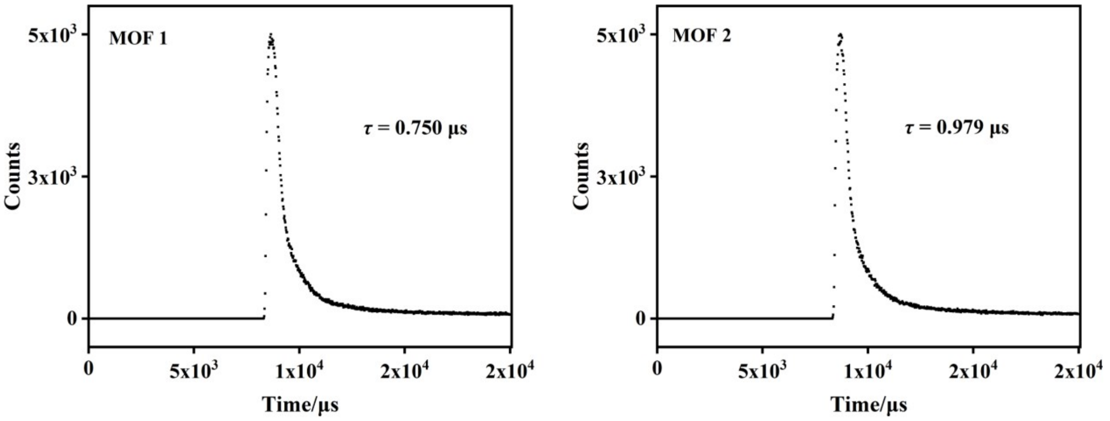

Fig. S6 Time resolved luminescence decay of **1** and **2**.

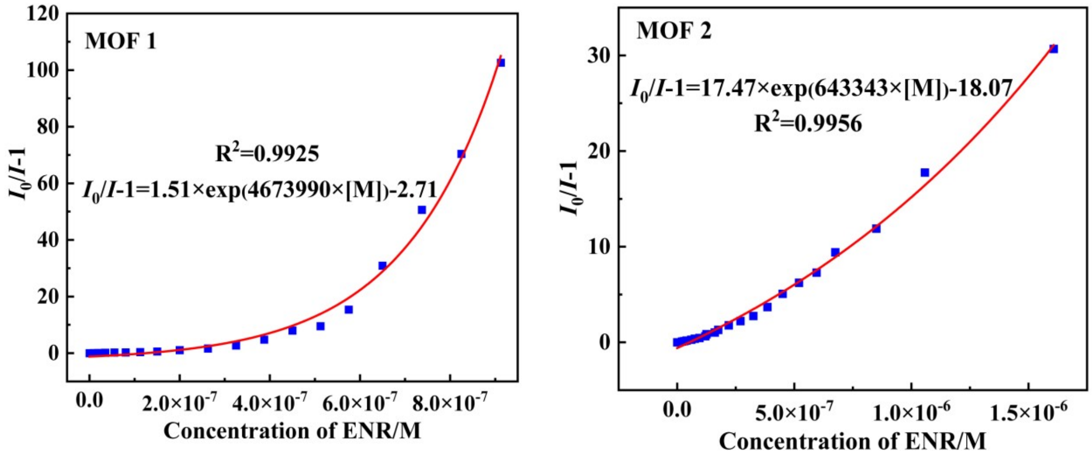

Fig. S7. The plots of relative **1**–**2** luminescence intensities *vs* enrofloxacin (ENR) concentration.

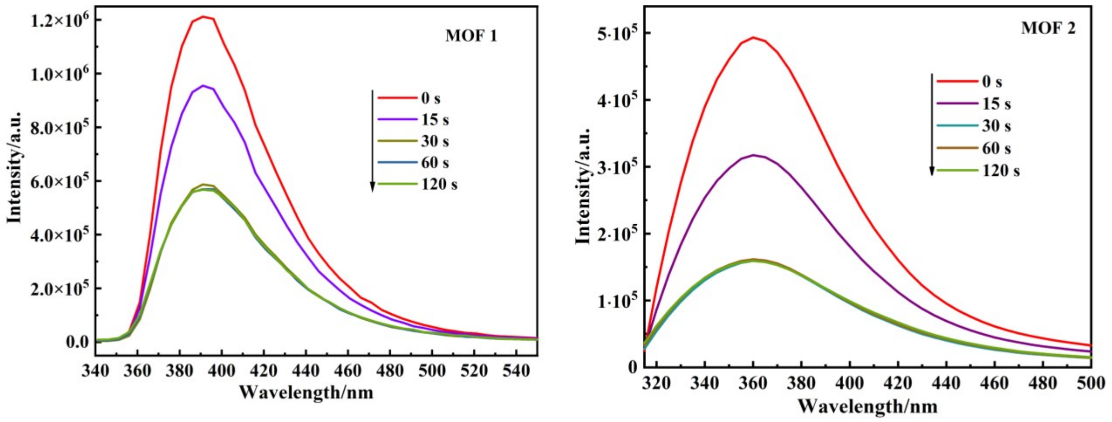

Fig. S8. Time-dependent emission spectra of **1**–**2** with ENR (0.25 μmol/L) at the different reaction time.

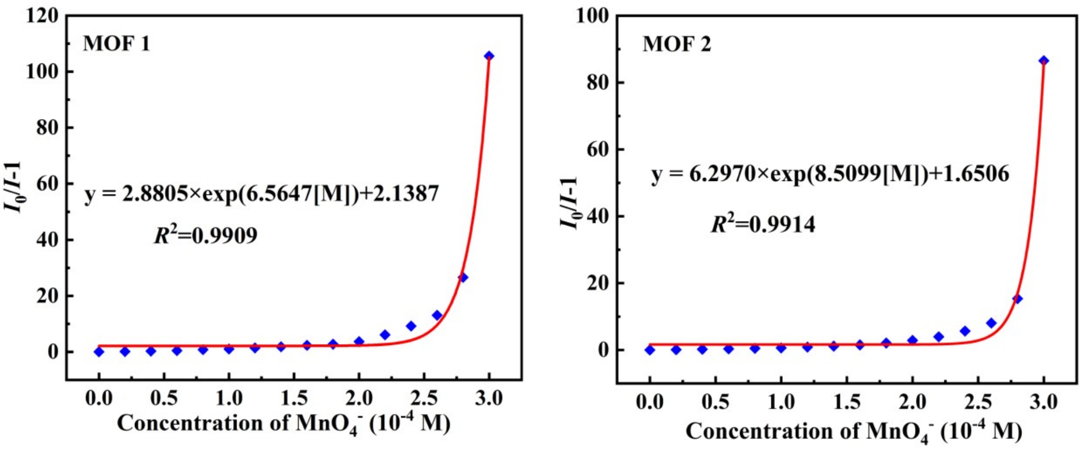

Fig. S9. The correlation curves between [(I_0/I) − 1] and the concentration of MnO_4^- obtained by the Stern−Volmer equation.

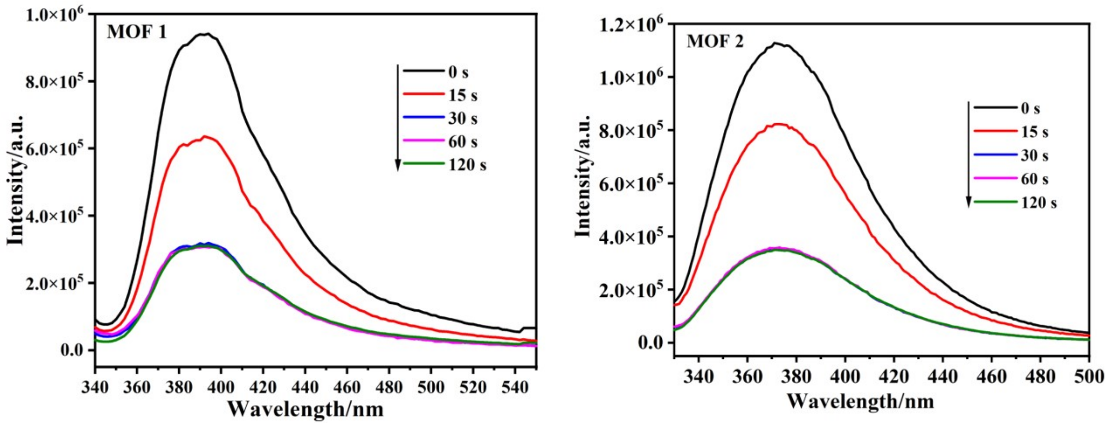

Fig. S10. The time required for the quenching efficiencies of **1**/**2**@MnO_4^- anions to reach the maximum.

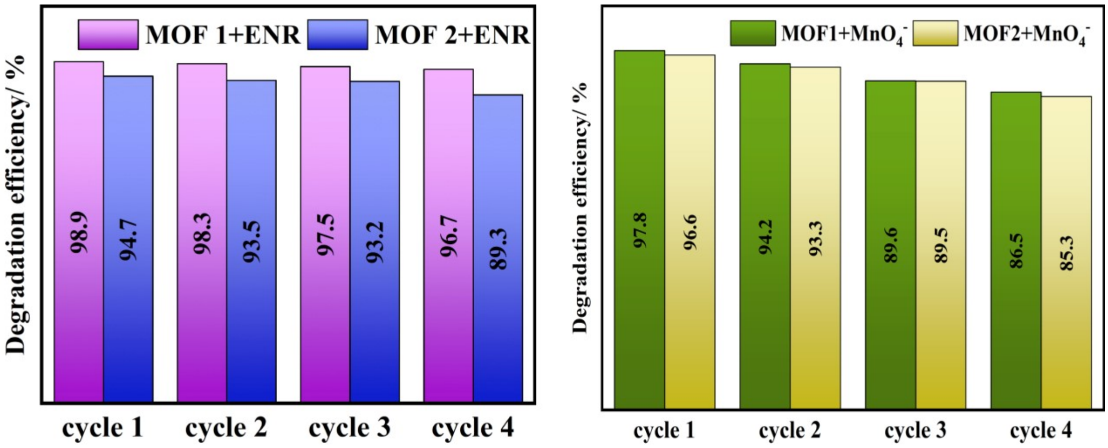

Fig. S11. Comparison of the quenching efficiencies of **1**–**2** for sensing of ENR/MnO_4^- anions over four cycles.

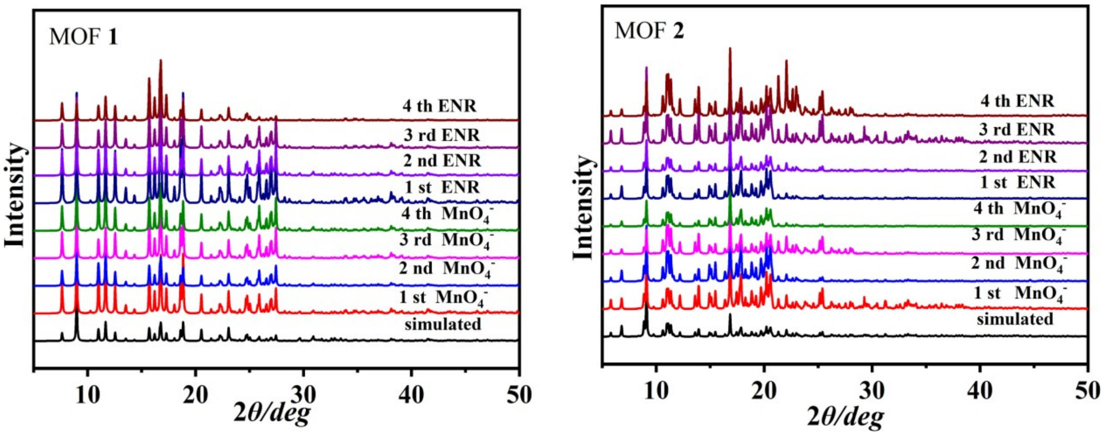

Fig. S12. PXRD patterns of **1**–**2** after 4 cycles of detecting of ENR/MnO$_4^-$ anions

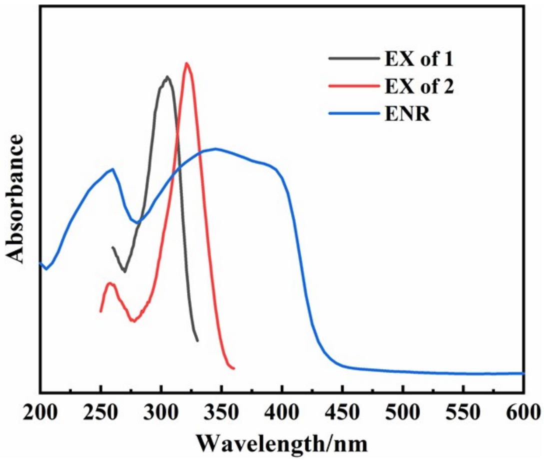

Fig. S13. Fluorescence excitation spectra of **1**/**2** and UV–vis absorption spectrum of enrofloxacin.

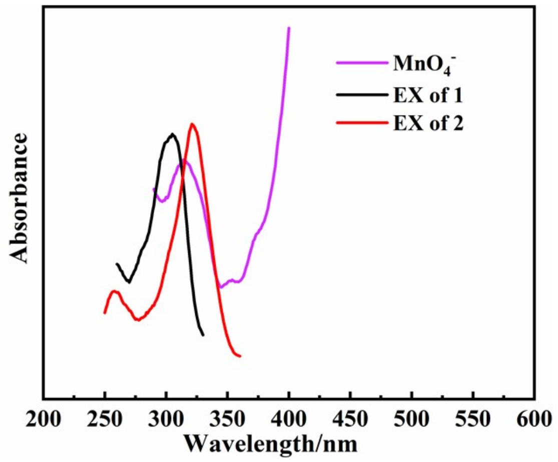

Fig. S14. Spectral overlap between the absorption spectrum of MnO_4^- anions and the excitation spectra of **1**–**2**.